

Ideal Strength and Intrinsic Ductility in Hexagonal Close Packed Metals From Second and Third Order Elastic Constants

(Dated: January 4, 2016)

Under tensile loading the ideal strength of a solid is governed by mechanical instabilities corresponding to failure in tension or shear, indicative of intrinsic brittle or ductile behavior, respectively. First principles-calculations for hexagonal close packed (hcp) metals under tensile loading along the c axis reveal that Be, Mg, Ru, Os and Zn fail in tension, while Sc, Y, Ti, Zr, Hf, Tc and Re fail in shear. An analytical model is developed that predicts this behavior in terms of the second and third order elastic constants. For the transition metals, filling of the d -bands is shown to correlate with the type of instability realized, thus providing unique insights into the effect of alloying on the intrinsic mechanical behavior of hcp metals.

I. INTRODUCTION

For a given loading condition, the ideal strength of a crystalline solid forms an upper bound on the mechanical stress that the material can sustain prior to reaching a mechanical instability. The nature of the instability reached at this stress level can provide insights into the intrinsic failure mechanisms for a material. For example, under tensile loading crack initiation requires that the local normal stress perpendicular to the cleavage plane is equal to or larger than the ideal tensile strength¹⁻⁴. However, when a material yields under tensile loading, it is possible for it to fail through a shear instability⁵⁻⁹. The tensile versus shear nature of the mechanical instability realized under tensile loading is of considerable interest as an indicator of whether a material will behave in an intrinsically brittle or ductile manner. For cubic metals, first-principles calculations of ideal strength under tensile loading have revealed shear instabilities for the ductile metals V and Nb, whereas more brittle materials such as W and Mo have been shown to fail in tension⁶. Similar studies in alloys¹⁰⁻¹³ have been undertaken recently, yielding insights into compositional effects. For example, it has been shown that BCC-based Mo-alloys can be made intrinsically more ductile by tuning the d band filling through alloying⁶.

In this work we consider the deformation behavior of the HCP metals, a class of materials that find use in diverse technological applications, spanning biomedical to automotive and aerospace. These materials can possess attractive properties such as high strength-to-weight ratios, high stiffness and/or high melting temperatures. However applications of these materials is often limited by low ductility, associated with the limited number of active slip systems in the HCP structure. Substantial efforts have been devoted to optimizing the ductility of HCP metals and alloys, for example by alloying and through the control of microstructure. Despite this significant body of work, the fundamental ideal strengths of HCP-metals have been reported for only a few systems¹⁴, and no attempts at using the results of such studies to derive insights into the intrinsic ductility of these materials, and how they may be altered through alloying, have been made to the best of our knowledge.

For the HCP metals Be, Mg, Sc, Y, Ti, Zr, Hf, Tc,

Re, Ru, Os and Zn, we compute the ideal strength and associated mechanical instabilities under tensile loading along the crystallographic c axis, i.e., perpendicular to the basal plane. This is a particularly important loading condition for the consideration of the intrinsic ductility of HCP metals, as the basal plane is a typical cleavage plane in these materials¹⁵, and slip of the dominant a -type dislocations does not provide a mechanism for plastic elongation along the c direction. Based on the ideal deformation behavior, each of the HCP metals is characterized as intrinsically brittle or ductile, i.e., as possessing elastic instabilities that are either tensile or shear in nature, respectively. We further study map out domains of d -band filling for HCP transition metals where ductile vs brittle behavior can be expected. Finally, we provide an analytical formalism which enables the ideal strength and the nature of the intrinsic instability under tensile loading along the c axis to be derived solely from a knowledge of the second and third-order elastic constants. The analytical model is shown to yield predictions in reasonable agreement with explicit density-functional-theory (DFT) calculations across all of HCP metals considered in this work, with reduced computational cost.

II. METHODOLOGY

A. Derivation of third-order elastic constants for different crystal systems

General derivation procedure goes here, both for cubic and hexagonal.

1. Cubic under uniaxial tension

State results for cubic symmetry C' for tension along c .

2. Hexagonal under uniaxial tension

State results for hexagonal symmetry C' for tension along c .

3. Do we want to include other symmetries?

B. Calculation of second and third-order elastic constants

The previous section has laid out a methodology to study elastic instabilities in HCP materials loaded in ten-

sion along the c axis, in terms of SOEC's and TOEC's. In this section, it is shown how these quantities can be calculated in a robust manner. By applying a set of carefully constructed deformations to a cell, all 10 independent TOEC's can be extracted by fitting the stress components, as calculated from DFT, to the applied strains. The pertinent expressions used in this work are given as follows:

$$t_1(\eta_1) = \rho_0 \frac{\partial E}{\partial \eta_1} \Big|_{\eta_2=\eta_3=\eta_4=\eta_5=\eta_6=0} = \frac{C_{111}\eta_1^2}{2} + C_{11}\eta_1 \quad (1)$$

$$t_2(\eta_2) = \rho_0 \frac{\partial E}{\partial \eta_2} \Big|_{\eta_1=\eta_3=\eta_4=\eta_5=\eta_6=0} = \frac{C_{222}\eta_2^2}{2} + C_{11}\eta_2 \quad (2)$$

$$t_3(\eta_3) = \rho_0 \frac{\partial E}{\partial \eta_3} \Big|_{\eta_1=\eta_2=\eta_4=\eta_5=\eta_6=0} = \frac{C_{333}\eta_3^2}{2} + C_{33}\eta_3 \quad (3)$$

$$t_3(\eta_1) = \rho_0 \frac{\partial E}{\partial \eta_3} \Big|_{\eta_2=\eta_3=\eta_4=\eta_5=\eta_6=0} = \frac{C_{113}\eta_1^2}{2} + C_{13}\eta_1 \quad (4)$$

$$t_1(\eta_3) = \rho_0 \frac{\partial E}{\partial \eta_1} \Big|_{\eta_1=\eta_2=\eta_4=\eta_5=\eta_6=0} = \frac{C_{133}\eta_3^2}{2} + C_{13}\eta_3 \quad (5)$$

$$t_2(\eta_1) = \rho_0 \frac{\partial E}{\partial \eta_2} \Big|_{\eta_2=\eta_3=\eta_4=\eta_5=\eta_6=0} = \frac{C_{112}\eta_1^2}{2} + C_{12}\eta_1 \quad (6)$$

$$t_4(\eta_4) = \rho_0 \frac{\partial E}{\partial \eta_4} \Big|_{\eta_1=\eta_2=\eta_3=\eta_5=\eta_6=0} = C_{44}\eta_4 \quad (7)$$

$$t_3(\eta_3, \eta_5) = \rho_0 \frac{\partial E}{\partial \eta_3} \Big|_{\eta_1=\eta_2=\eta_4=\eta_6=0} = \frac{C_{333}\eta_3^2}{2} + C_{33}\eta_3 + \frac{C_{344}\eta_5^2}{2} \quad (8)$$

$$t_5(\eta_3, \eta_5) = \rho_0 \frac{\partial E}{\partial \eta_5} \Big|_{\eta_1=\eta_2=\eta_4=\eta_6=0} = C_{44}\eta_5 + C_{344}\eta_3\eta_5 \quad (9)$$

$$t_3(\eta_1, \eta_2) = \rho_0 \frac{\partial E}{\partial \eta_3} \Big|_{\eta_3=\eta_4=\eta_5=\eta_6=0} = \frac{C_{113}\eta_1^2}{2} + C_{123}\eta_1\eta_2 + C_{13}\eta_1 + \frac{C_{113}\eta_2^2}{2} + C_{13}\eta_2 \quad (10)$$

$$t_4(\eta_1, \eta_4) = \rho_0 \frac{\partial E}{\partial \eta_4} \Big|_{\eta_2=\eta_3=\eta_5=\eta_6=0} = C_{44}\eta_4 + C_{144}\eta_1\eta_4 \quad (11)$$

$$t_5(\eta_1, \eta_5) = \rho_0 \frac{\partial E}{\partial \eta_5} \Big|_{\eta_2=\eta_3=\eta_4=\eta_6=0} = C_{44}\eta_5 + C_{155}\eta_1\eta_5 \quad (12)$$

where the following Voigt-notation is employed: 11 \mapsto 1, 22 \mapsto 2, 33 \mapsto 3, 23 \mapsto 4, 13 \mapsto 5, 12 \mapsto 6. In Eqs. 1-

12, t_i denotes components of the Lagrangian stress tensor, defined in terms of the true stress tensor components σ_i as given in Appendix B, ρ_0 is the mass density in the undeformed state, and E denotes the strain energy per unit mass¹⁶.

In the applications of Eqs. 1-12 to determine the SOEC's and TOEC's, strains are applied varying from -6 % to + 20%, in steps of 0.5 %, and the resulting true stresses and Lagrangian stresses are computed from the true stress tensor obtained by DFT¹⁶. Note that this strain range is considerably larger than what is commonly used for the calculation of the SOEC's. The TOEC's give rise to a nonlinear stress-strain behavior and this effect only becomes apparent at relatively large strains (larger than approximately 10 % for the materials studied in this work), hence the extended strain range.

The set of Eqs. 1-12 give rise to an overdetermined system that is solved for the 5 independent SOEC's and 10 independent TOEC's. A pseudo-inverse is employed, calculated from a singular value decomposition. The values of the calculated TOEC's are found in this work to be rather sensitive to the precise strain range that is employed in the fitting, which has been observed also in the literature¹⁶⁻¹⁸. For the HCP systems studied in this work, the TOEC's converge to a plateau when approximately 11-16 % maximum strain is used in the fit. Using smaller or larger maximum strains than those corresponding to the plateau can lead to TOEC's differing by up to a factor 5 for the systems studied in this work. For maximum strains within the plateau-region, TOEC's are generally converged to within 25 % in this work. Consistent with other work in the literature, the location of this plateau dictates which precise strain range is used in the fitting^{17,18}.

C. Wallace formalism and elastic instabilities

1. Cubic materials

Derive (analytical) expressions for failure point using Wallace tensor.

2. Hexagonal materials

This section has to be updated with our correct TOEC's

The elastic stability of a solid under zero stress is governed by the eigenvalues of its elastic-constant tensor; specifically, all 6 eigenvalues of this tensor must be larger than zero for the solid to be elastically stable. For a solid under an applied stress, elastic stability is governed instead by the Wallace tensor, defined as follows:

$$B_{ijkl} = C'_{ijkl} + \frac{1}{2} (\sigma_{il}\delta_{jk} + \sigma_{jl}\delta_{ik} + \sigma_{ik}\delta_{jl} + \sigma_{jk}\delta_{il} - 2\sigma_{ij}\delta_{kl}) \quad (13)$$

where C'_{ijkl} represents the elastic constants in the deformed configuration¹⁹⁻²¹, σ_{ij} denotes the applied stress acting on the solid, and δ_{ij} is the Kronecker-delta. The eigenvalues of the symmetrized Wallace tensor govern the elastic stability of a solid under stress²². In the present context, the symmetrized Wallace tensor, B_{sym} is defined as $B_{sym} = 1/2 (B + B^T)$ (with B given in Eq. 13), where the use of Voigt notation is implied so that both B and B_{sym} reduce to 6×6 matrices. In the remainder of this paper, the Wallace-tensor B_{ijkl} refers to the symmetrized Wallace tensor.

For the special case of an HCP structured material loaded in tension along the c axis, i.e., with only the stress component σ_{33} being non-zero, the Wallace tensor takes the following form:

$$B_{ijkl} = \begin{bmatrix} C'_{11} & C'_{12} & C'_{13} + \frac{\sigma_{33}}{2} & 0 & 0 & 0 \\ C'_{12} & C'_{11} & C'_{13} + \frac{\sigma_{33}}{2} & 0 & 0 & 0 \\ C'_{13} + \frac{\sigma_{33}}{2} & C'_{13} + \frac{\sigma_{33}}{2} & C'_{33} - \sigma_{33} & 0 & 0 & 0 \\ 0 & 0 & 0 & C'_{44} - \frac{\sigma_{33}}{2} & 0 & 0 \\ 0 & 0 & 0 & 0 & C'_{44} - \frac{\sigma_{33}}{2} & 0 \\ 0 & 0 & 0 & 0 & 0 & \frac{C'_{11} - C'_{12}}{2} \end{bmatrix} \quad (14)$$

where the terms C'_{ij} are the elastic constants in the deformed configuration. The eigenvalues of Eq. 14 determine the elastic stability of an HCP material under uniaxial tension along the c -axis. In this case there are 5 distinct eigenvalues, 3 of which involve the stress σ_{33} explicitly. From the 5 distinct eigenvalues, 2 are associated with a shear mode: $\lambda^{(1)} = C'_{44} - \frac{\sigma_{33}}{2}$ and $\lambda^{(2)} = \frac{1}{2} (C'_{11} - C'_{12})$. The other 3 eigenvalues ($\lambda^{(3)}$,

$\lambda^{(4)}$ and $\lambda^{(5)}$) relate to non-shear modes. In particular, $\lambda^{(3)}$ represents a tensile failure in the basal plane and is given as: $\lambda^{(3)} = (C'_{11} - C'_{12})$. Finally, $\lambda^{(4)}$ and $\lambda^{(5)}$ occur as a pair of solutions to a quadratic equation, with $\lambda^{(4)} < \lambda^{(5)}$. From these 5 eigenvalues, only the eigenvectors corresponding to $\lambda^{(4)}$ and $\lambda^{(5)}$ have a non-zero component along the c axis and hence, correspond to tensile failure along the loading direction. Since $\lambda^{(4)} < \lambda^{(5)}$,

$\lambda^{(4)}$ is the relevant eigenvalue governing tensile failure. The 2 eigenvalues considered in the remainder of this work are $\lambda_1 = \lambda^{(1)}$ and $\lambda_2 = \lambda^{(4)}$, see Eqs. 15 and 16. In principle, $\lambda^{(2)}$ and $\lambda^{(3)}$ have to be considered as well for the study of elastic instabilities. However these eigenvalues in fact increase along the deformation path for the materials and loading case studied in this paper and do not attain a value of zero. Hence, these do not contribute to elastic instabilities in the present case and will not be

considered further. This can be rationalized by considering the strain state of the materials and elastic constants of second and higher order (see below).

$$\lambda_1 = C'_{44} - \frac{\sigma_{33}}{2} \quad (15)$$

$$\lambda_2 = \frac{C'_{11} + C'_{12} + C'_{33} - \sigma_{33}}{2} - \frac{\sqrt{(C'^2_{11} + 2C'_{11}C'_{12} - 2C'_{11}C'_{33} + 2C'_{11}\sigma_{33} + C'^2_{12} - 2C'_{12}C'_{33} + 2C'_{12}\sigma_{33} + 8C'^2_{13} + 8C'_{13}\sigma_{33} + C'^2_{33} - 2C'_{33}\sigma_{33} + 3\sigma^2_{33})}}{2} \quad (16)$$

With increasing tensile stress, if λ_1 becomes negative before λ_2 , the crystal fails in shear, with the opposite case corresponding to failure in tension.

The eigenvalues given in Eq. 15 and 16 contain the elastic constants of the crystal in its deformed state. These can be obtained in principle by calculating the elastic tensor from DFT as a function of applied stress. However, this is a computationally expensive procedure that does not lead to a clear physical understanding of the underlying physics underlying the elastic instabilities. Alternatively, the elastic constants in the deformed configuration,

C'_{ij} , can also be approximated from the third order elastic constants (TOEC's) and the standard second order elastic constants at zero stress (SOEC's). The TOEC's dictate how the elastic constants C'_{ij} evolve as a function of the imposed strain. Let $\xi = \eta_{33}$ represent the (imposed) tensile strain along the c -axis of an HCP-materials and let $\eta = \eta_{11} = \eta_{22}$ be the resulting strain in the basal plane (usually contraction in accordance with a positive Poisson's ratio) corresponding to zero normal stress in these directions. For this strain state, the expressions for C'_{11} , C'_{12} , C'_{13} , C'_{33} and C'_{44} are given as follows 17^{23,24}:

$$C'_{11} = C_{11} + \eta(4C_{11} + 2C_{12} + C_{111} + C_{112}) + \xi(-C_{11} + 2C_{13} + C_{113}), \quad (17a)$$

$$C'_{12} = C_{12} + \eta(C_{111} + 2C_{112} - C_{222} + 2C_{12}) + \xi(-C_{12} + C_{123}), \quad (17b)$$

$$C'_{13} = C_{13} + \eta(C_{113} + C_{123}) + \xi(C_{13} + C_{133}), \quad (17c)$$

$$C'_{33} = C_{33} + \eta(4C_{13} - 2C_{33} + 2C_{133}) + \xi(5C_{33} + C_{333}), \quad (17d)$$

$$C'_{44} = C_{44} + \eta\left(\frac{1}{2}C_{11} + \frac{1}{2}C_{12} + C_{13} + C_{144} + C_{155}\right) + \xi\left(\frac{1}{2}C_{13} + \frac{1}{2}C_{33} + C_{44} + C_{344}\right) \quad (17e)$$

where the terms C_{ijk} denote the 10 independent TOEC's for the HCP-materials studied in this work^{25–28}. We now proceed by eliminating η from Eqs. 17 by expressing it in terms of ξ . As shown in Appendix A, from a third-order

expansion of the energy versus strain, it can be derived that this value of $\eta = \bar{\eta}$ for a given ξ can be obtained from the solution to the following equation:

$$\bar{\eta}^2(2C_{111} + 3C_{112} - C_{222}) + \bar{\eta}(C_{11} + 2C_{12} + 2C_{113}\xi + 2C_{123}\xi) + \xi^2C_{133} + 2\xi C_{13} = 0. \quad (18)$$

This resulting expression for $\bar{\eta}(\xi)$ is lengthy and is not

presented here. When this expression is substituted into

Eqs. 17, ξ becomes the only remaining (control) variable. The resulting expressions for C'_{ij} can be substituted into Eqs. 15 and 16 to determine which eigenvalue becomes negative first under applied strain, and the associated stress which defines the ideal strength.

To obtain the final closed-form expressions, we express the stress σ_{33} in terms of the strain state, SOEC's and TOEC's, using the relations given in Appendix B. An equation can then be set up to determine the value of the strain ξ , at which a shear instability first occurs; starting from Eq. 15, we substitute the expression for C'_{44} from Eq. 17, with ξ is the control variable and $\eta = \eta_1 = \eta_2 = \bar{\eta}$ the resulting contraction in the basal plane of the material, as given in Eq. 18, and σ_{33} specified from the expressions in Appendix II. Similarly, the strain ξ at which a tensile elastic instability occurs can be derived by considering the eigenvalue in Eq. 16 and substituting the expressions for C'_{ij} and σ_{33} . The smallest strain ξ at which an elastic instability (either shear or tensile) first occurs is indicated by $\bar{\xi}$ hereafter.

D. DFT-calculations

For the elemental metals all calculations were performed using the Vienna Ab Initio Simulation Package (VASP)^{29,30}. In these calculations use was made of the Perdew-Burke-Ernzerhof generalized gradient functional (PBE-GGA)³¹, and the projector augmented wave (PAW) method^{32,33}. An energy cutoff for the plane waves of 700 eV was used, and smearing of the electronic occupancies was performed using the Methfessel-Paxton scheme³⁴, with a broadening of 0.05 eV. Integrations in the Brillouin zone were carried out using Monkhorst-Pack k -point sampling³⁵ with a density chosen such that the number of k -points in the first Brillouin zone times the number of atoms in the cell equals approximately 25,000. The employed PAW potentials for Sc, Ti, Y, Zr and Hf include s and p semi-core states as valence electrons. For the other elements, only the outermost s and d -states are used as valence. The maximum calculated tensile stress σ_{33} that occurs along the deformation path (similar to the ultimate tensile strength) is converged to within approximately 2% with these DFT settings.

For the purpose of investigating d -band filling effects on ideal deformation behavior, we also employed calculations based on the virtual crystal approximation (VCA). The VCA calculations were performed using the Quantum Espresso software³⁶, employing norm-conserving Troullier-Martin pseudopotentials^{37,38}. Use was made of the generalized gradient approximation, based on the Perdew-Burke-Ernzerhof exchange-correlation functional³¹. The pseudopotentials were generated using the fhi98PP code with intermediate nuclear charges³⁹ to approximate a given alloy composition. The plane-wave cutoff, k -point sampling and broadening employed for these DFT calculations based on VCA are the same as those described earlier, employing PAW pseu-

dopotentials. The maximum calculated tensile stress for these calculations is converged to within approximately 3%.

E. Alloys and SQS generation

Describe SQS procedure here, also rationale for looking at Mo-Nb.

III. RESULTS AND DISCUSSION

In this section, results for HCP Be, Mg, Sc, Y, Ti, Zr, Hf, Tc, Re, Ru, Os and Zn are presented. Lattice stabilities are calculated as a function of the strain η_{33} along the c axis, and the failure modes are determined. This results in a categorization of the HCP metals considered into two classes: those that fail in shear (intrinsically ductile) or in tension (intrinsically brittle) for this loading condition. Further, the effect of d -band filling is studied on the failure modes for the HCP transition metals, leading to guidelines for the compositions where their solid solutions are expected to be intrinsically brittle or ductile for tensile loading along c .

A. Elastic instabilities in HCP materials: A comparison of direct DFT and analytical model results

The Wallace-tensor (see Eq. 14) can be approximated from the above formalism by means of the SOEC's and TOEC's. However, it also can be calculated explicitly from DFT for each strain along the c -deformation path. This direct DFT approach is expensive since for every strain along the c -axis, a structural relaxation of the lattice vectors in the basal plane, and the atomic coordinates, must be performed to give zero shear stresses, zero normal stresses within the basal plane, and zero forces. Further, a calculation of the elastic constants in the deformed configuration, C'_{ijkl} , is required for each such relaxed strained configuration, which further increases the computational cost. Such a direct approach to calculating the Wallace tensor and lattice instabilities is in principle more accurate than the analytical formalism based on the SOEC's and TOEC's, since it does not require the evaluation of the TOEC's and hence mitigates some of its associated inaccuracies. In this section, we present results based on both methods to compare the accuracy of the approaches.

Results are shown in Table I. The analytical model predicts the ideal failure mode (either shear or tensile failure) correctly for the 10 transition metals considered, as well as Zn, Cd, Be and Mg. Further, the critical c -axis strain ($\bar{\xi}$) at which an elastic instability first occurs is predicted to within an accuracy of approximately 4 %. The differences in $\bar{\xi}$ calculated directly from DFT and from

the analytical model can be attributed to two main factors. First, the calculation of TOEC's from DFT is prone to numerical errors, which will propagate through in the evaluation of $\bar{\xi}$. Second, in this work the strain energy is only expanded up to the third order in the strains. As strains increase, fourth-order terms would have to be included to increase numerical accuracy. Given the computational cost required to achieve numerically stable values of these higher-order elastic constants, the inclusion of these terms in the analytical models were not pursued in this work. We note that the discrepancies between the ideal strength predicted according to DFT and the analytical model are in reasonable agreement, with maximum errors comprising 50 %, in particular for the transition metals near half d -band filling. The possible explanation for this is again that for relatively large strains, higher-order elastic constants would have to be included in the model.

In this work it is found that out of the 12 HCP metals studied, 5 fail in tension: Ru, Os, Zn, Mg and Be and are categorized as intrinsically brittle, whereas the other 7 HCP metals are intrinsically ductile. The results in Table I are qualitatively in agreement with experiments, in which the ductility of Be, Os, Zn and Ru was characterized as poor, meaning less than 15 % elongation in a tensile test. Further, the ductility of Zr, Ti and Hf was characterized as good (elongation greater than 40 %) and finally the ductility of Y, Mg and Re was characterized as fair, indicating maximum elongations in between 15 % and 40 %¹⁵. It should be noted however that ductility is ultimately dictated by strength and work hardening. The calculations in this work provide only a way of gauging intrinsic ductility, thereby not taking into consideration extrinsic effects that largely govern the ductility of real materials. Therefore, care has to be taken to make comparisons with experimental data.

B. Elastic instabilities and d -band filling

The results in the previous section indicate that group III (Sc, Y), IV (Ti, Zr) and VII (Tc, Re) HCP transition metals fail in shear whereas group VIII (Ru, Os) HCP transition metals fail in tension when loaded in tension along the c axis. The formalism developed in this paper shows that second and third order elastic constants dictate the failure mode under this loading condition. Further, it is known that the d -band filling plays an important role in determining properties such as lattice constants, cohesive energies and elastic constants. Hence, it may be expected that the ideal strength behavior of the HCP transition metals may show systematic trends versus d -band filling. We explore this issue further in the present section, employing results obtained from VCA calculations.

The VCA is employed here to study the ideal strength behavior of alloys with d -band filling between groups i) III and IV, ii) VI and VII and iii) VII and VIII. By em-

ploying VCA-calculations, approximate ranges of d -band filling are mapped out in which shear versus tensile failure occurs. This leads to the map given in Fig. 1, of the periodic table showing band filling domains in which either intrinsically ductile (shear) or intrinsically brittle (tensile) failure are found to occur. We note that the group III and IV HCP transition metal alloys fail in shear, and the same holds true for all HCP alloys with d -band fillings in between. Further, group IV HCP metals can be alloyed with elements having d band fillings larger than those in group IV (e.g. Nb, Ta) and maintain intrinsically ductile behavior. However, there is a limit on how much d -band filling can be increased since i) the HCP-phase becomes energetically destabilized with respect to the BCC structure as the d -band filling moves towards group V, and ii) the HCP phase becomes mechanically unstable under zero stress as the d -band filling goes beyond a critical value. Fig. 1 suggests guidelines for the design of HCP transition metal alloys, by indicating approximate alloy compositional ranges that result in intrinsically ductile behavior, while maintaining mechanical stability at zero stress.

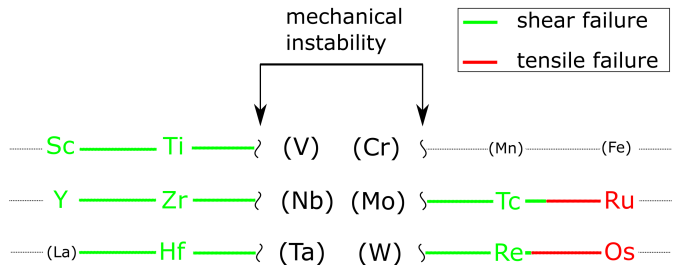


FIG. 1. Ideal failure mode-diagram vs. d -band filling in HCP metals and alloys

Moving to the right of the periodic table, we note that the group VII HCP-metals Re and Tc fail in shear and are hence intrinsically ductile. The metal Re is of particular interesting, as it exhibits the highest shear modulus among all HCP metals that fail in shear, suggesting the interesting combination of high strength and ductility. Moving further to the right, we note the metals Ru and Os in group VIII, exhibiting the highest shear moduli among all HCP-metals and almost all other elements in the periodic table. These fail in tension when loaded along c , largely due to their very high shear moduli. Small perturbations in d -band filling towards lower values do not change the ideal deformation behavior and the intrinsically brittle failure mode is maintained all the way up to d -band fillings close to group VII.

The formalism based on SOEC's and TOEC's developed in this work can be used to understand the features of the elastic response underlying shear versus tensile failure. Consider first HCP materials with high shear moduli, C_{44} , such as Ru and Os. These materials are not likely to fail in shear, since the eigenvalue associated with shear failure (Eq. 15) is rather large and may not

TABLE I. Calculated SOEC's, TOEC's and ideal-failure characteristics for 12 HCP metals. Failure modes are characterized as either shear (S) or tension (T).

	Sc	Y	Ti	Hf	Zr	Tc	Re	Ru	Os	Zn	Mg	Be
SOEC's (GPa)												
C_{11}	100	77	174	182	145	489	618	554	733	166	59	306
C_{12}	37	25	81	72	64	225	275	181	227	36	29	32
C_{13}	29	27	75	69	66	192	224	176	225	35	20	15
C_{44}	29	25	43	52	25	171	159	175	248	30	17	165
C_{33}	71	61	183	20	161	534	677	613	801	71	67	406
TOEC's (GPa)												
C_{133}	-117	-143	-273	-214	-146	-1014	-1557	-1220	-1408	-21	-1808	-318
C_{333}	-230	-303	-1078	-1463	-1173	-4004	-5715	-5980	-7955	-797	-4625	-4347
C_{111}	-734	-529	-1584	-1567	-1301	-4771	-6786	-5758	-7764	-2179	-5247	-2407
C_{112}	-83	-24	10	-120	103	-526	-1020	-656	-828	-57	-1531	-81
C_{113}	-50	-58	169	-22	169	6	107	-621	-604	31	432	59
C_{222}	-691	-475	-1173	-1354	-961	-4175	-6103	-5263	-7146	-2862	-5043	-1887
C_{123}	-219	-185	-661	-237	-494	-1768	-712	-275	-332	-498	-1886	-7
C_{144}	-15	8	170	-260	218	-1100	-451	-417	-562	-227	-964	-332
C_{155}	37	58	-34	-154	49	-126	-519	-566	-801	-351	8	-88
C_{344}	-135	-128	-246	-460	-162	-1061	-1281	-930	-1297	-234	-727	-726
Failure characteristics												
ξ (direct DFT)	0.22	0.20	0.19	0.14	0.19	0.18	0.19	0.15	0.15	0.12	0.22	0.17
ξ (analytical)	0.30	0.26	0.24	0.20	0.15	0.19	0.24	0.18	0.19	0.13	0.24	0.16
σ_{id} (GPa) (direct DFT)	13	9	15	12	11	44	54	48	62	5	6	24
σ_{id} (GPa) (analytical)	11	8	13	10	8	36	44	33	42	3	5	20
Failure mode	S	S	S	S	S	S	S	T	T	T	T	T

reach zero before the eigenvalue in Eq. 16. Hence, this observation explains from an ideal strength point of view why the HCP metals that are most stiff in shear, and thus expected to have high strength, tend to be brittle under c -axis loading. Strong materials with a high shear modulus C_{44} will only fail in shear and be accordingly intrinsically ductile according to Eq. 15 if σ_{33} is relatively large in magnitude, requiring that C_{33} is large. Further, the modulus C_{333} is negative for most materials, implying softening of C_{33} as the materials is strained along c by ξ . A small magnitude of C_{333} is also favorable for shear failure as it causes the magnitude of the stress σ_{33} decrease less rapidly as a function of ξ .

Metals and alloys near half d -band filling, such as Re and Tc, are intrinsically ductile and fail in shear but are on the border of d -band filling regions where tensile failure occurs. Their shear failure is caused by an interplay of the SOEC's and TOEC's. First, the shear moduli C_{44} of Re and Tc are large but smaller than those for Os and Ru. The same is true for the moduli C_{33} , but the ratio C_{33}/C_{44} for group VII metals is larger than for group VIII: for Os $C_{33}/C_{44} \approx 3.2$ whereas for Re $C_{33}/C_{44} \approx 4.5$. Second, for group VII metals, the magnitude of C_{333} is smaller than for group VIII, which also promotes shear failure over tensile failure. Third, the TOEC C_{344} , which is a negative quantity for most materials, is relatively large in magnitude for group VII metals, relative to those in group VIII. According to Eq. 17 (e), this implies that the shear modulus C_{44} decreases relatively rapidly with strain ξ , which according to Eq. 15, favors a shear instability over a tensile instability.

Finally, the high ductility HCP metals in group IV exhibit values of C_{33}/C_{44} between approximately 4 and 6 which is higher than for groups VII and VIII. The relatively low values for C_{44} causes the eigenvalue in Eq. 15 to attain negative values before the eigenvalue in Eq. 16, and consequently to fail in shear.

IV. SUMMARY AND CONCLUSIONS

In this work, the ideal deformation behavior and elastic stabilities of 12 HCP metals under uniaxial stress along the c -axis are studied: Be, Mg, Sc, Y, Ti, Zr, Hf, Tc, Re, Ru, Os and Zn. It is found that out of these, 5 fail in tension along c (Be, Mg, Ru, Os and Zn) whereas the 7 others (Sc, Y, Ti, Zr, Hf, Tc and Re) fail in shear. This leads to a natural division of the HCP metals into 2 classes: those that are intrinsically ductile (i.e., fail in shear) or intrinsically brittle (i.e., fail in tension) under tensile loads along c . Using a formalism based on the expansion of the elastic energy to third order in strain, it is further shown that the critical strain and the deformation mode can be predicted from the relative magnitudes of these of the second and third order elastic constants. It is found that HCP metals exhibiting high moduli C_{44} tend to fail in tension rather than shear and hence, are intrinsically brittle. This occurs for transition metals and alloys in group VIII (Os, Ru). The HCP metals in groups III and IV are found to be intrinsically ductile under c -axis loading, primarily due to their low shear moduli C_{44} , which promotes shear failure. The group VII HCP met-

als (Re, Tc) are an interesting case that combine a high shear modulus with intrinsically ductile behavior. The physical reason for this behavior is the specific combination of SOEC's and TOEC's that this class of materials exhibits: a high C_{33} , but a relatively small magnitude of C_{333} and a large magnitude of C_{344} . Finally, the trends of the ideal deformation behavior with d -band filling are revealed, resulting in approximate d -electron counts per atom for which an alloy is expected to fail in a ductile or brittle mode.

Appendix A

The imposed strain along c (ξ) and the resulting strain in the basal plane (η) required to ensure zero normal stress within the basal plane are related by the Poisson's ratio for small strains. For large values of ξ , however, the TOEC's have to be invoked to calculate η .

Consider the mapping between the reference and current configuration of a continuum solid. In the reference configuration, a particle occupies a point \mathbf{p} with spatial coordinates $\mathbf{X} = X_1\mathbf{e}_1 + X_2\mathbf{e}_2 + X_3\mathbf{e}_3$, where $\mathbf{e}_1, \mathbf{e}_2, \mathbf{e}_3$ is a Cartesian reference triad and X_1, X_2, X_3 are the reference coordinates. Upon deformation of the body, the point originally at \mathbf{X} is translated by the displacement vector $\mathbf{u}(X_1, X_2, X_3)$ to its final coordinates $\mathbf{x}(X_1, X_2, X_3)$, see Eq. A1.

$$\mathbf{x}(X_1, X_2, X_3) = \mathbf{u}(X_1, X_2, X_3) + \mathbf{X}(X_1, X_2, X_3) \quad (\text{A1})$$

Based on this description, a deformation gradient is formulated as in Eq. A2. The Green-Lagrange strain tensor $\boldsymbol{\eta}$ then follows from \mathbf{F} as shown in Eq. A3, where \mathbf{I} denotes the identity matrix.

$$\mathbf{F} = \frac{\partial \mathbf{x}_i}{\partial X_j} \quad (\text{A2})$$

$$\boldsymbol{\eta} = \frac{1}{2} (\mathbf{F}^T \mathbf{F} - \mathbf{I}) \quad (\text{A3})$$

With the notation now established, the strain energy density can be expanded in terms of the SOEC's, TOEC's and the Green-Lagrange strain as in Eq. A4, where ρ_0 represents the mass density in the undeformed state and the terms η_i represent the components of the tensor defined in Eq. A3. The symmetry of the SOEC's and TOEC's will be applied in the expansions, which simplifies the resulting expressions considerably.

$$\rho_0 E(\boldsymbol{\eta}) = \frac{1}{2!} \sum_{i,j=1}^6 C_{ij} \eta_i \eta_j + \frac{1}{3!} \sum_{i,j,k=1}^6 C_{ijk} \eta_i \eta_j \eta_k + \dots \quad (\text{A4})$$

Consider an imposed strain ξ along the c -axis of an HCP-metal, initially keeping all other dimensions fixed to the zero strain-state. Consider first the expansion of Eq.

A4, retaining only terms up to and including the SOEC's (hence, ignoring the TOEC's for now). This gives the energy-expression in Eq. A5, in which the symmetry of the SOEC's has been applied. To obtain the equilibrium strain in the basal plane due to the application of ξ , we perform strain energy-minimization and set $\bar{\eta} = \eta = \eta_1 = \eta_2, \eta_3 = \xi$ and $\eta_4 = \eta_5 = \eta_6 = 0$ in Eq. A5 and solve $\frac{\partial(\rho_0 E)}{\partial \eta}|_{\xi} = 0$. We find the equilibrium strain $\eta = \bar{\eta}$, given in Eq. A6, where the minus-sign signifies the Poisson-contraction in the basal plane.

$$\rho_0 E(\boldsymbol{\eta}) = C_{11} \frac{\eta_1^2}{2} + C_{11} \frac{\eta_2^2}{2} + C_{33} \frac{\xi^2}{2} + C_{44} \frac{\eta_4^2}{2} + C_{44} \frac{\eta_5^2}{2} + \frac{1}{2} (C_{11} - C_{12}) \frac{\eta_6^2}{2} + C_{12} \eta_1 \eta_2 + C_{13} \eta_1 \xi + C_{13} \eta_2 \xi \quad (\text{A5})$$

$$\eta = \bar{\eta} = -\frac{\xi C_{13}}{C_{11} + C_{12}} \quad (\text{A6})$$

For large strains, the expansion in Eq. A5 is not sufficient and instead, TOEC's have to be included as well. The expansion of the strain energy up to the third order in strain is given in Eq. A7, in which the terms P are given in Eq. A8. Note that in Eq. A7, the symmetry of the SOEC's and TOEC's has been incorporated to simplify the resulting expression.

$$\begin{aligned} \rho_0 E(\boldsymbol{\eta}) = & C_{11} P_1 + C_{12} P_2 + C_{13} P_3 + C_{33} P_4 + \\ & C_{44} P_5 + C_{111} P_6 + C_{222} P_7 + C_{333} P_8 + \\ & C_{133} P_9 + C_{113} P_{10} + C_{112} P_{11} + C_{123} P_{12} + \\ & C_{144} P_{13} + C_{155} P_{14} + C_{344} P_{15} \end{aligned} \quad (\text{A7})$$

$$P_1 = \frac{\eta_1^2}{2} + \frac{\eta_2^2}{2} + \frac{\eta_6^2}{4}, \quad (\text{A8a})$$

$$P_2 = -\frac{\eta_6^2}{4} + \eta_1 \eta_2, \quad (\text{A8b})$$

$$P_3 = \eta_1 \eta_3 + \eta_2 \eta_3, \quad (\text{A8c})$$

$$P_4 = \frac{\eta_3^2}{4}, \quad (\text{A8d})$$

$$P_5 = \frac{\eta_4^2}{2} + \frac{\eta_5^2}{2}, \quad (\text{A8e})$$

$$P_6 = \frac{\eta_1^3}{6} + \frac{\eta_1 \eta_2^2}{2} - \frac{\eta_1 \eta_6^2}{4} + \frac{\eta_2 \eta_6^2}{4}, \quad (\text{A8f})$$

$$P_7 = \frac{\eta_2^3}{6} - \frac{\eta_1 \eta_2^2}{2} - \frac{\eta_2 \eta_6^2}{8} + 3 \frac{\eta_1 \eta_6^2}{8}, \quad (\text{A8g})$$

$$P_8 = \frac{\eta_3^3}{6}, \quad (\text{A8h})$$

$$P_9 = \frac{\eta_1 \eta_3^2}{2} + \frac{\eta_2 \eta_3^2}{2}, \quad (\text{A8i})$$

$$P_{10} = \frac{\eta_3 \eta_1^2}{2} + \frac{\eta_3 \eta_2^2}{2} + \frac{\eta_3 \eta_6^2}{4}, \quad (\text{A8j})$$

$$P_{11} = \frac{\eta_1^2 \eta_2}{2} + \frac{\eta_1 \eta_2^2}{2} - \frac{\eta_6^2 \eta_1}{8} - \frac{\eta_6^2 \eta_2}{8}, \quad (\text{A8k})$$

$$P_{12} = \eta_1 \eta_2 \eta_3 - \frac{\eta_3 \eta_6^2}{4}, \quad (\text{A8l})$$

$$P_{13} = \frac{\eta_1 \eta_4^2}{2} + \frac{\eta_2 \eta_5^2}{2} - \frac{\eta_4 \eta_5 \eta_6}{2}, \quad (\text{A8m})$$

$$P_{14} = \frac{\eta_2 \eta_4^2}{2} + \frac{\eta_1 \eta_5^2}{2} + \frac{\eta_4 \eta_5 \eta_6}{2}, \quad (\text{A8n})$$

$$P_{15} = \frac{\eta_3 \eta_4^2}{2} + \frac{\eta_3 \eta_5^2}{2} \quad (\text{A8o})$$

Given an applied ξ , we can again find an analytical expression for the Poisson contraction $\eta = \bar{\eta}$ in terms of ξ and the SOEC's and TOEC's. The resulting equation that has to be solved is shown in Eq. 18. Solving Eq. 18

in terms of $\eta = \bar{\eta} = \eta_1 = \eta_2$ gives the equilibrium strain in the basal plane.

Appendix B

A simple expression for the relations between strains and stresses can be derived for an HCP-structured material that is loaded in tension along the c -axis, while allowing for contraction in the basal plane. For this situation, with an applied (Lagrangian) strain η_3 along c , we have $\eta_1 = \eta_2 = \bar{\eta}$ and $\eta_3 = \xi$. Eq. B1 expresses the Lagrangian stress tensor in terms of the strain energy and Lagrangian strain tensor¹⁶. From Eq. B1, the Lagrangian stress t_{33} can be found under the combined strain state currently under investigation, see Eq. B2. Further, from Eq. B3, we have that $\boldsymbol{\sigma} = \frac{1}{\det(\mathbf{F})} \mathbf{F} \mathbf{t} \mathbf{F}^T$ which governs the relation between Lagrangian and true stress. This expression can be expanded, with the result given in Eq. B4, where t_{33} is given in Eq. B2.

$$t_{ij} = \rho_0 \frac{\partial E}{\partial \eta_{ij}} \quad (\text{B1})$$

$$t_{33} \Big|_{\eta_4=\eta_5=\eta_6=0} = \eta_1^2 (C_{113} + C_{123}) + \eta_1 (2C_{13} + 2C_{133}\eta_3) + \frac{1}{2} C_{333} \eta_3^2 + C_{33} \eta_3 \quad (\text{B2})$$

$$t_{ij} = \det(\mathbf{F}) \mathbf{F}^{-1} \boldsymbol{\sigma} (\mathbf{F}^T)^{-1} \quad (\text{B3})$$

$$\sigma_{33} = \frac{\sqrt{2\xi+1}}{\sqrt{2\bar{\eta}+1}} t_{33} \quad (\text{B4})$$

-
- ¹ T. Li, J. Morris Jr, N. Nagasako, S. Kuramoto, and D. Chrzan, Physical review letters **98**, 105503 (2007).
² D. Clatterbuck, D. Chrzan, and J. Morris, Acta Materialia **51**, 2271 (2003).
³ A. Kelly and N. H. Macmillan, Oxford University Press, Walton Street, Oxford OX 2 6 DP, UK, 1986. (1986).
⁴ H. Wang and M. Li, Physical review letters **111**, 065507 (2013).
⁵ D. M. Clatterbuck, C. R. Krenn, M. L. Cohen, and J. W. Morris, Phys. Rev. Lett. **91**, 135501 (2003).
⁶ L. Qi and D. Chrzan, Phys. Rev. Lett. **112**, 115503 (2014).
⁷ N. Macmillan, in *Atomistics of fracture* (Springer, 1983) pp. 95–165.
⁸ D. Roundy and M. L. Cohen, Physical Review B **64**, 212103 (2001).
⁹ H. Wang and M. Li, Journal of Physics: Condensed Matter **21**, 455401 (2009).

- ¹⁰ D. Roundy, C. R. Krenn, M. L. Cohen, and J. W. Morris, Phys. Rev. Lett. **82**, 2713 (1999).
¹¹ X. Li, S. Schönecker, J. Zhao, B. Johansson, and L. Vitos, Phys. Rev. B **87**, 214203 (2013).
¹² M. Šob, L. Wang, and V. Vitek, Materials Science and Engineering: A **234**, 1075 (1997).
¹³ F. Milstein and S. Chantasiriwan, Phys. Rev. B **58**, 6006 (1998).
¹⁴ L. Fu, Q. Zhang, and B. Y. Tang, in *Advanced Materials Research*, Vol. 476 (Trans Tech Publ, 2012) pp. 2523–2529.
¹⁵ M. Yoo, Metallurgical Transactions A **12**, 409 (1981).
¹⁶ M. Łopuszyński and J. A. Majewski, Physical Review B **76**, 045202 (2007).
¹⁷ H. Wang and M. Li, Physical Review B **79**, 224102 (2009).
¹⁸ H. Wang and M. Li, Physical Review B **85**, 104103 (2012).

- ¹⁹ D. C. Wallace, Thermodynamics of crystals (Courier Corporation, 1998).
- ²⁰ J. R. Ray, *Computer physics reports* **8**, 109 (1988).
- ²¹ J. Wang, S. Yip, S. Phillpot, and D. Wolf, *Physical Review Letters* **71**, 4182 (1993).
- ²² J. Wang, J. Li, S. Yip, S. Phillpot, and D. Wolf, *Physical Review B* **52**, 12627 (1995).
- ²³ R. R. Rao and R. Srinivasan, *physica status solidi (b)* **31**, K39 (1969).
- ²⁴ R. R. Rao, *Physical Review B* **10**, 4173 (1974).
- ²⁵ R. Hearmon, *Acta Crystallographica* **6**, 331 (1953).
- ²⁶ M. Rose and R. Ramsey, *physica status solidi (b)* **25**, 103 (1968).
- ²⁷ F. G. Fumi, *Physical Review* **83**, 1274 (1951).
- ²⁸ F. G. Fumi, *Physical Review* **86**, 561 (1952).
- ²⁹ G. Kresse and J. Furthmüller, *Phys. Rev. B* **54**, 11169 (1996).
- ³⁰ G. Kresse and J. Hafner, *Phys. Rev. B* **47**, 558 (1993).
- ³¹ J. P. Perdew, K. Burke, and M. Ernzerhof, *Phys. Rev. Lett.* **77**, 3865 (1996).
- ³² P. E. Blöchl, *Phys. Rev. B* **50**, 17953 (1994).
- ³³ G. Kresse and D. Joubert, *Phys. Rev. B* **59**, 1758 (1999).
- ³⁴ M. Methfessel and A. T. Paxton, *Phys. Rev. B* **40**, 3616 (1989).
- ³⁵ H. J. Monkhorst and J. D. Pack, *Phys. Rev. B* **13**, 5188 (1976).
- ³⁶ P. Giannozzi, S. Baroni, N. Bonini, M. Calandra, R. Car, C. Cavazzoni, D. Ceresoli, G. L. Chiarotti, M. Cococcioni, I. Dabo, et al., *Journal of Physics: Condensed Matter* **21**, 395502 (2009).
- ³⁷ N. Troullier and J. L. Martins, *Physical Review B* **43**, 1993 (1991).
- ³⁸ L. Romaner, C. Ambrosch-Draxl, and R. Pippan, *Phys. Rev. Lett.* **104**, 195503 (2010).
- ³⁹ M. Fuchs and M. Scheffler, *Computer Physics Communications* **119**, 67 (1999).